Nanostructured Aluminium Hydroxyfluorides Derived from β-AlF_3

Damien Dambournet,[†] Alain Demourgues,*[,†] Charlotte Martineau,[§,||] Stanislas Pechev,[†] Jérôme Lhoste,[†] Jérôme Majimel,[†] Alexandre Vimont,[‡] Jean-Claude Lavalley,[‡] Christophe Legein,[§] Jean-Yves Buzaré,[||] Franck Fayon,[⊥] and Alain Tressaud[†]

Institut de Chimie de la Matière Condensée de Bordeaux-CNRS, Université Bordeaux 1, 87 Avenue du Dr. A. Schweitzer, 33608 Pessac cedex, France, Laboratoire Catalyse et Spectrochimie, UMR 6506, CNRS-ENSICAEN-Université de Caen, Boulevard du Maréchal Juin, F-14050 Caen Cedex, France, Laboratoire des Oxydes et Fluorures, CNRS UMR 6010, IRIM2F, CNRS FR 2575, Université du Maine, Avenue Olivier Messiaen, 72085 Le Mans Cedex 9, France, Laboratoire de Physique de l'Etat Condensé, CNRS UMR 6087, IRIM2F, CNRS FR 2575, Université du Maine, Avenue Olivier Messiaen, 72085 Le Mans Cedex 9, France, and Centre de Recherche sur les Matériaux à Haute Température, CNRS UPR 4212, 1D Avenue Recherche Scientifique, 45071 Orléans Cedex 2, France

Received September 12, 2007. Revised Manuscript Received December 3, 2007

Microwave-assisted synthesis has been applied for the preparation of aluminum hydroxyfluorides derived from β-AlF_3. In the course of obtaining high-surface-area and homogeneous nanocrystallites, several key parameters have been adjusted. A relationship between the OH/F molar ratio and the stabilized allotropic forms has been pointed out. The surface area has been monitored depending on the water/isopropanol volume ratio. The microstructural properties of the as-prepared material have been thoroughly investigated highlighting X-ray line broadening arising from strains and size effects. It has been concluded from X-ray diffraction data refinements and TEM results that the prepared crystallites possess a platelet shape with an average particle size of 15 nm associated with a high surface area of 82 m^2 g^{-1}. The occurrence of hydroxyl groups inside the network has been detected by FTIR spectroscopy and considered angles and bond distances are probably located in peculiar crystallographic sites, i.e., 8f (F1) and 16h (F2) Wyckoff positions. ^{19}F NMR as well as ^{27}Al high-field NMR spectroscopies are powerful tools to probe and quantify the various $AlF_{6-x}(OH)_x$ environments and confirm the preferential location of OH groups in 8f (F1) and 16h (F2) Wyckoff positions. A preliminary study using NH_3 adsorption revealed the occurrence of strong Lewis acid sites on the surface of β-$AlF_{3-x}(OH)_x$.

1. Introduction

Because of their high catalytic activity toward the halogen exchange reaction,[1] aluminum fluorides have been extensively investigated in the way that they assist the conversion of ozone-depleting[2] CFCs compounds in more environmentally acceptable compounds: HFCs. The Al−F system gives rise to numerous allotropic forms.[3] In addition to the thermodynamically stable phase α-AlF_3[3a] (space group $R\bar{3}c$) derived from the ReO_3 type structure, β-AlF_3 is the most known phase because it possesses high catalytic properties.[4] The structure has been solved by Le Bail et al.[3c] and derives from the hexagonal tungsten bronze (HTB) structure that consists of AlF_6 octahedra linked by corners and forming along the *c* direction channels with hexagonal section (Figure 1). This phase is metastable and therefore requires a multistep synthesis that conventionally consists of a thermal degrada-

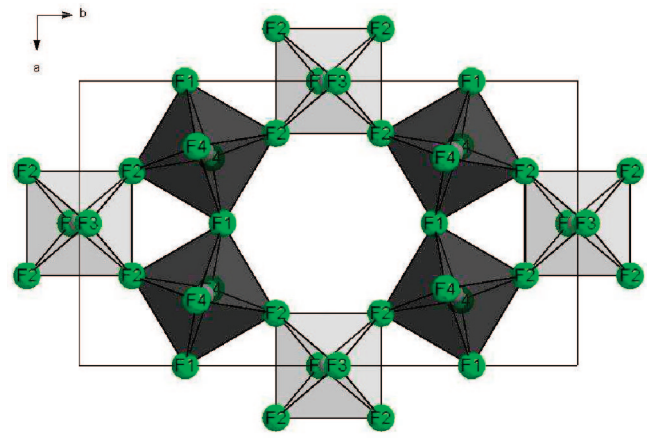

Figure 1. Network of the β-AlF_3 type structure: view along the *c* axis. The octahedra in light and dark grey denote Al1 and Al2 atom types, respectively.

* Corresponding author. E-mail: demourgues@icmcb-bordeaux.cnrs.fr.
[†] ICMCB–CNRS, Université Bordeaux 1.
[‡] Université de Caen.
[§] Laboratoire des Oxydes et Fluorures, Université du Maine.
[||] Laboratoire de Physique de l'Etat Condensé, Université du Maine.
[⊥] Centre de Recherche sur les Matériaux à Haute Température.

(1) Kemnitz, E.; Menz, D. H. *Prog. Solid State Chem.* **1998**, *26*, 97.
(2) *Fluorine and the Environment: Atmospheric Chemistry, Emissions, and Lithosphere*; Advances in Fluorine Science Series; Tressaud, A., Ed.; Elsevier: Amsterdam, 2006; Vol. 1.
(3) (a) Daniel, P.; Bulou, A.; Rousseau, M.; Nouet, J.; Fourquet, J. L.; Leblanc, M.; Burriel, R. *J. Phys.: Condens. Matter* **1990**, 5663. (b) Fourquet, J. L.; Rivière, M.; Le Bail, A. *Eur. J. Solid State Inorg. Chem.* **1988**, *25*, 535. (c) Le Bail, A.; Jacoboni, C.; Leblanc, M.; De Pape, R.; Duroy, H.; Fourquet, J. L. *J. Solid State Chem.* **1988**, *77*, 96. (d) Herron, N.; Thorn, D. L.; Harlow, R. L.; Jones, G. A.; Parise, J. B.; Fernandez-Baca, J. A.; Vogt, T. *Chem. Mater.* **1995**, *7*, 75. (e) Le Bail, A.; Fourquet, J. L.; Bentrup, U. *J. Solid State Chem.* **1992**, *199*, 151. (f) Ravez, J.; Mogus-Milankovic, A.; Chaminade, J. P.; Hagenmuller, P. *Mater. Res. Bull.* **1984**, *19*, 1311. (g) Chupas, P. J.; Chaudhuri, S.; Hanson, J. C.; Qui, X.; Lee, P. L.; Shastri, S. D.; Billinge, S. J. L.; Grey, C. P. *J. Am. Chem. Soc.* **2004**, *126*, 4756.
(4) Hess, A.; Kemnitz, E. *J. Catal.* **1994**, *149*, 449.

10.1021/cm702603b CCC: $40.75
Published on Web 01/31/2008

tion[5] of either ammonium fluoride salts (NH_4AlF_4, $(NH_4)_3AlF_6$) or aluminum trihydrate (α-$AlF_3 \cdot 3H_2O$). Unfortunately, these routes give rise to low specific surface area materials ($\sim$30 $m^2\ g^{-1}$), which drastically limits their reactivity because of a small number of active surface sites. Because of the strong electronegativity of the fluoride ions, new routes have been developed consisting either of non aqueous sol–gel[6] or plasma[7,8] fluorination processes leading to X-ray amorphous AlF_3 exhibiting high-surface-area powders (>200 and 190 $m^2\ g^{-1}$, respectively). At the same time, progress in computer calculation has enabled the improvement of theoretical surface structure and reconstruction. Wander et al. have investigated the β-AlF_3 (001) surface terminations, highlighting the occurrence of undercoordinated Al^{3+} environments, which are assumed to act as strong Lewis acid sites.[9,10] Moreover, using atomistic molecular dynamic simulations, Chaudhuri et al.[11] have shown that significant surface reconstruction occurs on cubic α-AlF_3 nanoparticles, also leading to strongly undercoordinated Al^{3+} environments, i.e., Lewis acid centers. It was therefore of great interest to develop a new route enabling the synthesis of materials presenting nanosized crystallized particles, i.e., with high surface area.

With this aim, the nonconventional route using microwave irradiation as a heating source has been used in moderate hydrothermal conditions. This peculiar process results from the interaction between the electrical field component and the matter and gives rise to two mechanisms,[12] i.e., dipolar–polarization and ionic conduction, allowing us to generate heat in the core of the solution and not transmit it through the vessel. A large number of advantages as compared to the conventional route are listed in the literature and can be summarized as follows: stabilization of novel as well as metastable phases, improvement of reaction kinetics, energy efficiency. These advantages constitute a promising area of research.[13] Some authors have already proved that this route can be used for the synthesis of well-crystallized metal fluorides through ionic liquid decomposition[14] (Fe, Co, Zn, La, Y, Sr) or novel hydride metal fluorides.[15] We report here the direct synthesis using microwave irradiation of nanosized metastable β-AlF_3 containing hydroxyl groups. The key synthesis parameters to obtain pure nanosized β-$AlF_{3-x}(OH)_x$ are presented. An accurate characterization of the samples is carried out through X-ray diffraction, FTIR spectroscopy, BET measurement, transmission electron microscopy, and ^{27}Al and ^{19}F NMR spectroscopy.

2. Experimental Section

2.1. Microwave Synthesis and Determination of the Chemical Composition. Syntheses were performed using a MARS-5 Microwave Digestion System (CEM Corp.). Temperature was regulated by percent increments of the microwave power (300 W, 2.45 GHz frequency) and controlled by an optic fiber. Internal pressure was measured by a pressure sensor. In a first step, a precursor solution was prepared as follows: 12.5 mmol of Al(III) nitrate (Sigma-Aldrich, 98% $Al(NO_3)_3 \cdot 9H_2O$) was dissolved in a water/isopropanol solution (10 mL of distilled water/10 mL of isopropanol, Sigma-Aldrich, 98%). An aqueous solution of HF (Panreac 40%) was then added in order to get an [HF]/[Al] precursor molar ratio equal to 3, which led to the precipitation of α-$AlF_3 \cdot 3H_2O$. The final volume solution did not exceed 22 mL. The precursor was placed in a closed Teflon container for microwave hydrothermal synthesis (XP-1500 plus model). Two steps were used during this process. First, the solution was heated at 373 K (288 K/min) for 10 min and then at 433 K for 2 h. The first step was required because of the occurrence of a side reaction induced by microwave irradiation: an exothermic phenomenon leading to an increase in the temperature and an internal pressure reaching about 443 K and 16–18 bar, respectively, which took place after 5 min of irradiation. The origin of this phenomenon will be discussed latter.

After heat treatment, a microwave-assisted drying was performed under a primary vacuum and argon flow at 373 K. The powder was then washed with a large amount of ethanol under nitrogen pressure and finally outgassed at 573 K under a vacuum for 4 h.

The final [F]/[Al] molar ratio was measured by electron probe microanalysis (Castaing microprobe CECAMA SX 630 apparatus) using F^- titration with specific electrode and Al^{3+} by ICPMS at the CNRS Central Service of Analysis. Although it was very difficult to get an accurate determination of the [F]/[Al] ratio, the obtained data led to a value close to 2.5 ($\pm$ 0.1) whatever the water/isopropanol solution ratio used. Considering the electroneutrality equation, this value of the [F]/[Al] molar ratio led us to consider the occurrence of hydroxyl groups stabilized within the network. This hypothesis was further confirmed by FTIR spectroscopy and will be discussed in the following. A chemical composition could thus be considered for the β phase series: $AlF_{2.5}(OH)_{0.5} \cdot xH_2O$, x being determined by thermogravimetric analysis and found in the range of 0.1–0.2. To simplify the chemical formula, the water content will not be indicated in the following.

2.2. X-ray Diffraction Analysis. Powder diffraction patterns were recorded on a PANalytical X'Pert Pro diffractometer in a Bragg–Brentano geometry ($\theta-2\theta$), using Ge(111) monochromated Cu $K\alpha_1$ radiation (λ = 1.54051Å). The investigated 2θ range was 10–110° with a step of 0.017°.

The whole pattern profile matching and the Rietveld structural refinement were performed with the FULLPROF program.[16] Individual peak profile analysis was carried out using PROFILE, version 1.4 (Socabin, Bruker AXS).

2.3. Surface Area Measurement. N_2 adsorption isotherms were performed at 77 K using an ASAP 2000 instrument from Micromeritics. The powder sample of mass around 200 mg was evacuated overnight at 573 K under 0.1 Pa prior to adsorption. The specific surface area S_{BET} was calculated from BET results applied in the P/P_o (0.03–0.25) range. The estimated standard deviation (esd) has been calculated for surface areas larger than 30 $m^2\ g^{-1}$ and is equal to 5 $m^2\ g^{-1}$.

(5) Francke, L.; Durand, E.; Demourgues, A.; Vimont, A.; Daturi, M.; Tressaud, A. *J. Mater. Chem.* **2003**, *13*, 2330.
(6) Kemnitz, E.; Groβ, U.; Rudiger, S.; Shekar, C. S. *Angew. Chem., Int. Ed.* **2003**, *42*, 4251.
(7) Delattre, J. L.; Chupas, P. J.; Grey, C. P.; Stacy, A. M. *J. Am. Chem. Soc.* **2001**, *123*, 5364.
(8) Hajime, E. K. L. Y.; Delattre, J. L.; Stacy, A. M. *Chem. Mater.* **2007**, *19*, 894.
(9) Wander, A.; Bailey, C. L.; Searle, B. G.; Mukhopadhyay, S.; Harrison, N. M. *Phys. Chem. Chem. Phys.* **2005**, *7*, 3989.
(10) Wander, A.; Bailey, C. L.; Mukhopadhyay, S.; Searle, B. G.; Harrison, N. M. *J. Mater. Chem.* **2006**, *16*, 1906.
(11) Chaudhuri, S.; Chupas, P.; Morgan, B. J.; Madden, P. A.; Grey, C. P. *Phys. Chem. Chem. Phys.* **2006**, *8*, 5045.
(12) Kappe, C. O. *Angew. Chem., Int. Ed.* **2004**, *43*, 6250.
(13) Adam, D. *Nature* **2003**, *421*, 571.
(14) Jacob, D. S.; Bitton, L.; Grinblat, J.; Felner, I.; Koltypin, Y.; Gedanken, A. *Chem. Mater.* **2006**, *18*, 3162.
(15) Thanh, S. P.; Gaslain, F.; Leblanc, M.; Maisonneuve, V. *J. Fluorine Chem.* **2000**, *101*, 161.
(16) Rodríguez-Carvajal, J. *Physica B* **1993**, *192*, 55.

2.4. Scanning Electron Microscopy. SEM pictures were obtained with a FX 600 microscope. Surface charge elimination was achieved by silver deposition.

2.5. Transmission Electron Microscopy. Transmission electron microscopy (TEM) was performed on a TECNAI F20 equipment with a field emissive gun, operating at 200 kV and with a point resolution of 0.24 nm. Fast Fourier transforms (FFT) of high-resolution transmission electron microscopy (HRTEM) images were calculated using the Gatan Digital Micrograph software. TEM samples were prepared by dissolving a few milligrams of powder in ethanol. The solution was then dipped 10 min into an ultrasonic bath so as to disagglomerate powder particles. One drop of the solution was finally deposited on a Formvar/carbon copper grid.

2.6. FTIR Spectroscopy. Infrared transmission spectra were recorded on self-supporting wafers (2 cm^2, 20 mg), which were placed into an infrared quartz cell (KBr windows) connected to a vacuum line. Samples were activated under vacuum at 573 K for one night. Spectra were recorded with a resolution of 4 cm^{-1}. The IR spectrometer was a Nicolet Nexus apparatus equipped with an extended KBr beam splitter and a mercury cadmium telluride (MCT) detector. Gaseous ammonia was dried on molecular sieves prior to use.

2.7. NMR Spectroscopy. Quantitative ^{19}F Hahn echo Magic Angle Spinning (MAS) NMR spectra were acquired on an Avance 300 Bruker spectrometer ($B_0 = 7$ T), using a 2.5 mm ^{19}F optimized CP MAS probe, operating at a ^{19}F Larmor frequency of 282.2 MHz. The 90° and 180° pulse durations were set to 4 μs (RF field 60 kHz) and 8 μs, respectively, with an interpulse delay equal to one rotor period. The recycle delay was taken to 10 s. The ^{19}F chemical shifts were referenced to $CFCl_3$ at 0 ppm. These spectra were reconstructed using the DMFIT software,[17] which allows a full reconstruction of the spectra (including the spinning sidebands) with six adjustable parameters: isotropic chemical shift δ_{iso}, chemical shift anisotropy δ_{aniso}, chemical shift asymmetry parameter η_{CS}, line width, relative line intensity, and line shape. In this study, the δ_{iso} values, the relative line intensities, and the line widths are the relevant parameters; the other parameters are not discussed at all in the following.

^{27}Al ($I = 5/2$) MAS NMR spectra were recorded using a 2.5 mm CP MAS probe at spinning speed 30–32 kHz on an Avance 750 Bruker spectrometer ($B_0 = 17.6$ T) and an Avance 300 Bruker spectrometer ($B_0 = 7$ T) operating at a ^{27}Al Larmor frequency of 195.5 and 78.2 MHz, respectively. A short pulse length of 1 μs was used to ensure quantitative excitation of the whole spin system. The recycle delay was set to 1 s and 4096 fids were accumulated. ^{27}Al spectra were referenced to a 1 M aqueous solution of $Al(NO_3)_3$. Quantitative reconstructions[18–21] of the central lines of the ^{27}Al NMR spectra were achieved taking into account the $N = 0$ spinning sideband of the satellite transitions $\langle 3/2 \rangle$ and the $N = 0$ spinning sideband of the central transition $\langle 1/2 \rangle$, which completely overlap. For each ^{27}Al NMR site, the isotropic chemical shift δ_{iso} and the quadrupolar product $\nu_{Q\eta}$ were calculated by comparison of the center of gravity $\delta_{cs}^{\langle 3/2 \rangle}$ of the Al satellite sideband with that of the central transition $\delta_{cs}^{\langle 1/2 \rangle}$, through the following equation

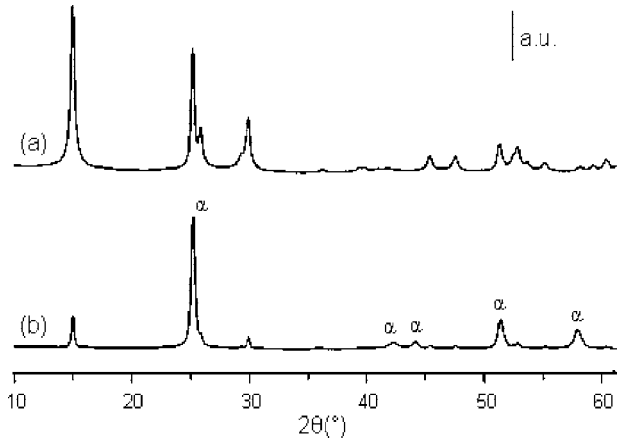

Figure 2. Effect of the aluminium precursor on the final product: X-ray diffraction powder pattern of material prepared from (a) aluminium nitrate and (b) aluminium chloride.

$$\delta_{cs}^{\langle m \rangle} = \delta_{iso} - \nu_{Q\eta}^2 \frac{[I(I+1) - 3 - 9m(m-1)]}{30\nu_0^2} \times 10^6$$

where $I = 5/2$ in the case of ^{27}Al, $\nu_0 = 195.5$ MHz (for the 17.6 T spectrometer) and $\nu_{Q\eta} = \nu_Q\sqrt{1+\eta_Q^2/3}$.[20]

^1H Hahn echo MAS NMR spectra were acquired on an Avance 300 Bruker spectrometer ($B_0 = 7$ T), using a 2.5 mm ^{19}F optimized CP MAS probe, operating at a Larmor frequency of 300 MHz for ^1H. They result in a broad unresolved peak between 0 and 10 ppm (referenced to ^1H in TMS at 0 ppm) that did not aid our analysis. These spectra are then neither shown nor discussed in the following.

3. Results and Discussion

3.1. Key Parameters of the Microwave-Assisted Route toward High-Surface-Area (HSA) β-$AlF_{3-x}(OH)_x$. *3.1.1. Nature of the Aluminum Precursor: Influence on the Final Allotropic Forms and Occurrence of a Secondary Reaction during the Microwave Process.* The effect of the Al^{3+} precursor has been investigated by comparing, in the conditions described above, aluminum nitrate (Sigma-Aldrich, 98% $Al(NO_3)_3 \cdot 9H_2O$) and aluminum chloride (Sigma-Aldrich, 98% $AlCl_3 \cdot 9H_2O$) precursor. The powder X-ray diffraction patterns of the as-prepared samples are shown in Figure 2. Pure β phase could be prepared by using nitrate precursor, in good agreement with JCPDS-ICDD file 84–1672, whereas the chloride precursor led to the stabilization of the thermodynamically stable phase α-AlF_3 (JCPDS-ICDD file 44–0231) as the major phase. As previously introduced, the use of nitrate as precursor leads to secondary reactions, which are characterized by an increase in the temperature and the pressure inside the vessel. Microwave-assisted synthesis is known to be able to induced side reactions. For instance, nitric acid was used to study the kinetics of the decomposition of organic substances under microwave irradiation. [22] One can assume that the reaction implying nitrate and isopropanol must be involved in the exothermic phenomenon observed. To confirm this hypothesis, we first recovered the

(17) Massiot, D.; Fayon, F.; Capron, M.; King, I.; Le Calvé, S.; Alonso, B.; Durand, J.-O.; Bujoli, B.; Gan, Z.; Hoatson, G. *Magn. Reson. Chem.* **2002**, *40*, 70.
(18) Massiot, D.; Bessada, C.; Coutures, J. P.; Taulelle, F. *J. Magn. Reson.* **1990**, *90*, 231–242.
(19) Alemany, L. B.; Massiot, D.; Sherriff, B. L.; Smith, M. E.; Taulelle, F. *Chem. Phys. Lett.* **1991**, *177*, 301–306.
(20) Massiot, D.; Müller, D.; Hübert, Th.; Schneider, M.; Kentgens, A. P. M.; Coté, B.; Coutures, J. P.; Gessner, W. *Solid State Nucl. Magn. Reson.* **1995**, *5*, 175–180.
(21) Stebbins, J. F.; Kroeker, S.; Lee, S. K.; Kiczenski, T. J. *J. Non-Cryst. Solids* **2000**, *275*, 1–6.
(22) Kubrakova, I. V.; Khamizov, R. Kh. *Russ. Chem. Bull., Int. Ed.* **2005**, *54*, 1413–1417.

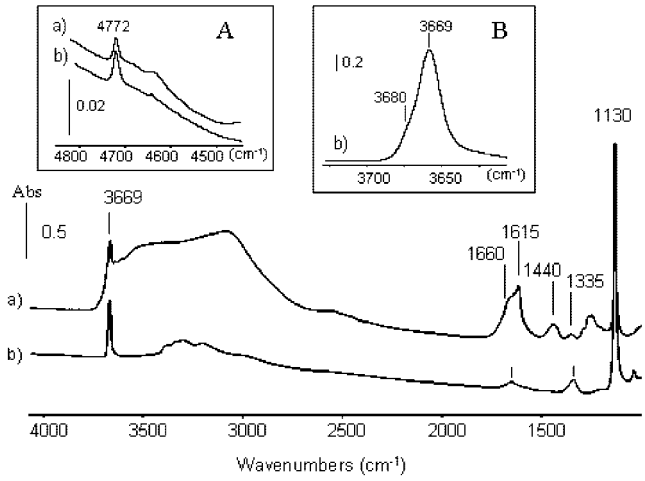

Figure 3. Infrared spectra of HSA β-$AlF_{3-x}(OH)_x$ (a) before and (b) after activation at 573 K. (Inset A: ($\delta+\nu$)OH region. Inset B: ν(OH) region).

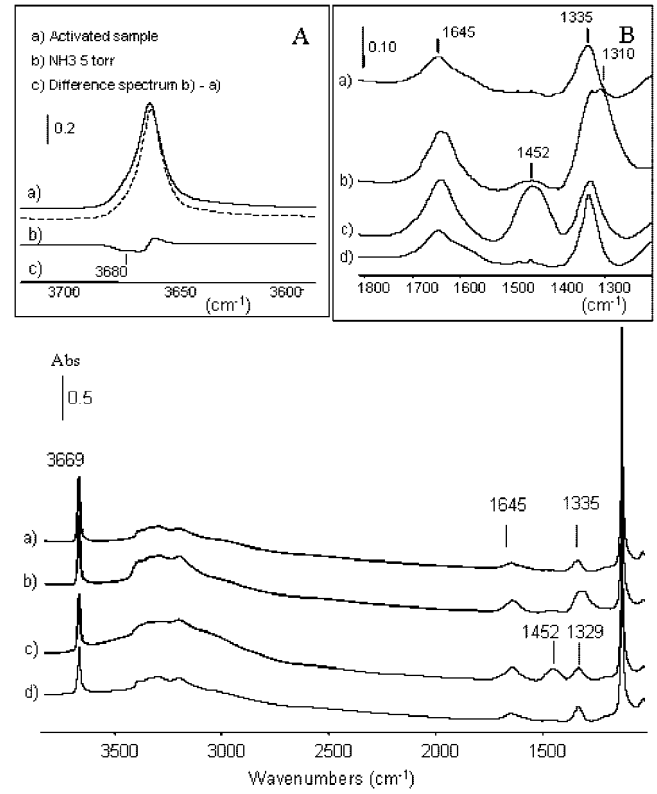

Figure 4. Infrared spectra of HSA β-$AlF_{3-x}(OH)_x$ recorded (a) after activation at 573 K, (b) after introduction of 5 Torr of NH_3 followed by evacuation at RT, (c) after introduction of $P_e = 1$ Torr of water followed by evacuation at RT, and (d) after evacuation at 573 K. Inset A: ν(OH) region. Inset B: zoom on the 1800–1250 cm^{-1} region.

remaining filtrate after microwave-assisted synthesis for analysis using a coupled gas chromatography/mass spectrometry performed by the CNRS Central Service of Analysis (SCA Vernaison). The analysis showed the presence of acetone and other products, which confirmed that isopropanol was oxidized during the synthesis.

It was interesting to then identify the redox couple at the origin of the partial oxidative process. In this aim, FTIR spectroscopy was performed on a sample prepared from nitrate, i.e., pure β-$AlF_{3-x}(OH)_x$. IR spectra of the sample before and after activation at 573 K are displayed in Figure 3. The IR spectrum of the sample before any activation (Figure 3a) exhibits many bands due to either bulk vibration or surface groups with impurities like water. After activation at 573 K, the latter is almost removed. According to Vimont et al., [23] the bands detected at 4772, 3669, and 1130 cm^{-1} are ascribed to $\nu+\delta$(OH), ν(OH), and δ(OH) of bridged Al−OH, respectively, confirming the presence of OH groups substituting fluoride ions into the network.

Before activation, supplementary bands are observed in particular in the 1700–1200 cm^{-1} region (Figure 3a). They could be due to adsorbed water or to impurities resulting from the synthesis mode. The occurrence of a weak band at 5270 cm^{-1} (not shown) unambiguously reveals the presence of water ($\nu+\delta(H_2O)$ mode). Therefore, the band at 1615 cm^{-1} with a shoulder at about 1660 cm^{-1} mainly characterizes the $\delta(H_2O)$ mode of water species, which are also responsible for the broadband near 3200 cm^{-1} ($\nu(H_2O)$).

Nevertheless, other bands like those at 1440 and 1335 cm^{-1} cannot be assigned to adsorbed water. Taking into account the preparation mode of the sample, nitrate-derived species could be considered. Infrared band frequencies of nitrate species depend on their structure. In particular, bridged species are characterized by a couple of $\nu(NO_3)$ bands near 1200 and 1600–1650 cm^{-1}. After activation at 573 K, two bands are still present at 1335 and 1645 cm^{-1} in addition to a broadband between 3400 and 3000 cm^{-1} (Figure 3b). Taking into account that the latter unambiguously characterizes the presence of NH_x species, we can deduce from the frequency of the bands at 1345 and 1635 cm^{-1} the occurrence of coordinated NH_3 species.

To check such an assignment, NH_3 has been adsorbed on the activated sample (Figure 4b). It is clear that the intensity of all NH_x bands has notably increased, confirming the presence of residual ammonia species onto the activated sample. The band near 1330 cm^{-1} is assigned to the $\delta s(NH_3)$ mode of coordinated NH_3 species; its frequency increases with the strength of the coordination sites.[24] Its position at 1335 cm^{-1} in the spectrum of the activated sample reveals the presence of very strong Lewis acid sites, in agreement with previous results on the β phase.[24] The strength of the NH_3 coordination is such that activation under a vacuum at 573 K is not sufficient to completely eliminate NH_3 species that can be localized on the outer surface or trapped into the HTB channels during the synthesis process. Ammonia addition at room temperature gives rise to a supplementary $\delta s(NH_3)$ band at 1310 cm^{-1} (Figure 4b, inset B), revealing the presence of weaker Lewis acid on the surface. Furthermore, the inset B of Figure 4d shows that evacuation at 573 K eliminates the NH_3 coordinated species adsorbed on these sites.

The addition of ammonia at room temperature gives also rise to a weak band at 1452 cm^{-1} assigned to ammonium

(23) Vimont, A.; Lavalley, J. C.; Francke, L.; Demourgues, A.; Tressaud, A.; Daturi, M. *J. Phys. Chem. B* **2004**, *108*, 3246.

(24) Busca, G. *Phys. Chem. Chem. Phys.* **1999**, *1*, 723.

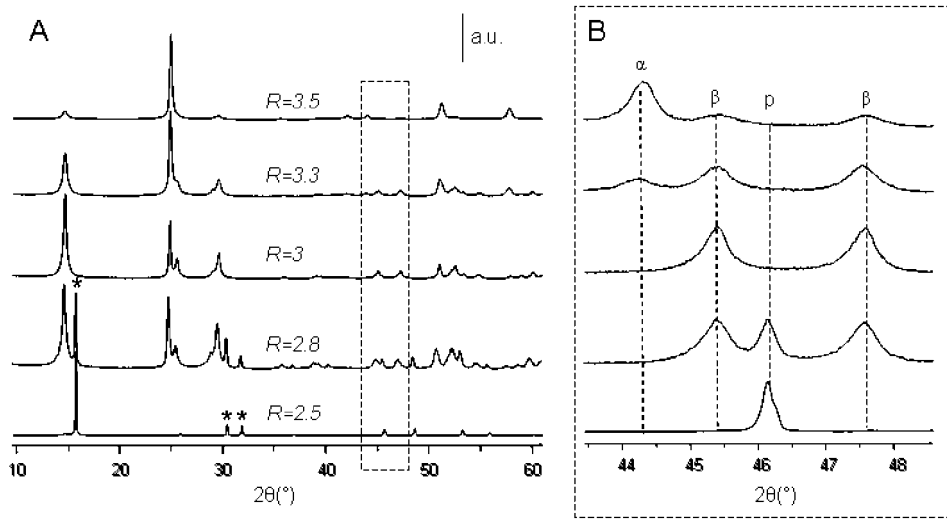

Figure 5. Evolution of the X-ray diffraction powder patterns as a function of the R = [HF]/[Al] precursor molar ratio: (A) global view where asterisks account for the main lines of the pyrochlore phase, (B) zoom, α, β, and p are assigned to α-AlF_3, β-AlF_3, and pyrochlore type structures, respectively.

species (Figure 4b, inset B). The formation of such species requires the presence of surface hydroxyl groups or residual water species. The difference spectrum before and after NH_3 adsorption at room temperature (Figure 4c, inset A) reveals the presence of a shoulder near 3680 cm^{-1}, which disappears after NH_3 sorption, whereas the strong band at 3669 cm^{-1} is not perturbed. NH_3 sorption has then highlighted the presence of surface OH groups on the activated sample; their frequency (3680 cm^{-1}), which is slightly higher than that of the bulk OH groups (3669 cm^{-1}), has been ascribed to the absence of the confinement effect occurring in the bulk. [24]

Water addition on the sample precovered with NH_3 leads to an increase in the intensity of the band at 1452 cm^{-1} because of the ammonium species, whereas the other band at 1310 cm^{-1} decreases (Figure 4c). This result shows that water converts NH_3 coordinated species into ammonium species and explains why the intensity of the 1440 cm^{-1} band is relatively intense in the spectrum of the nonactivated sample (Figure 3a).

Therefore, FTIR spectroscopy clearly shows that nitrate is reduced during the synthesis into ammonium ions. Furthermore, the thermodesorption of ammonium species shows the presence of strong Lewis acid sites. The importance of such species acting as initiators of the synthesis of the HTB-type structure is clearly illustrated in the present hydrothermal process. The exothermic redox reaction involving NO_3^- as the oxidizer and isopropanol as the reducing agent plays a key role in this synthesis, with the help of ammonium ions as templates for the stabilization of pure β-$AlF_{3-x}(OH)_x$. It is a similar process that occurs in conventional routes, i.e., the thermal degradation of either hydrate $AlF_3 \cdot 3H_2O$ or ammonium aluminum hexafluoride $(NH_4)_3AlF_6$,[5] in which molecules such as water or ammonium ions are involved in the formation of HTB-type structure.

3.1.2. [HF]/[Al] Precursor Molar Ratio: Relationships between the OH/F Content and the Nature of the Final Allotropic Form. To optimize the synthesis results, we varied the R = [HF]/[Al] precursor molar ratio from 2.5 to 3.5 using aluminum nitrate as precursor and a water/isopropanol solvent ratio equal to 1. Figure 5 shows the evolution of the powder X-ray diffraction patterns as a function of the [HF] content. Three domains can be distinguished: (i) for $R < 3$, (ii) $R = 3$, and (iii) $R > 3$. For lower ratio values, i.e., R = 2.5, hydroxyfluorides exhibiting the pyrochlore type structure with the $AlF_{1.5}(OH)_{1.5} \cdot xH_2O$ chemical composition[3b] are obtained as the major phase; an increase in the [HF] concentration up to $R = 2.8$ leads to a mixture of two phases: the β and pyrochlore forms. As described in the synthesis procedure, pure β form could be obtained using a precursor molar ratio equal to 3. Finally, higher [HF] contents lead to the appearance of the α-AlF_3 phase as an impurity. A zoom on the 43–49° 2θ range is presented in Figure 5B; it clearly shows the crucial influence of the [HF] content on the nature of the stabilized phase. This part of the diffractogram also accounts for the phase purity because in the 23–25° 2θ range, the α-AlF_3 main line cannot be clearly distinguished, because of the proximity of the β (002) reflection line.

Table 1. Correlation between the Al−X−Al angles and Building Units Present in the Hydroxy-Fluorides Series

phase	Al−X−Al (X = F or OH) bond angles (deg)	building units (*n*-membered rings)
α-AlF_3	158	4
β-AlF_3	148–148–166	3−6−4
pyrochlore $AlF_{1.5}(OH)_{1.5}$	141	3−6

The structural sequence of these various phases can be also related to the number of hydroxyl groups inside the framework, which is strongly dependent on the [HF]/[Al] precursor molar ratio. It appears that for increasing amounts of HF, the presence of fluoride ions favors, in a first step, the formation of the pyrochlore $AlF_{1.5}(OH)_{1.5}$, then β-$AlF_{3-x}(OH)_x$, and finally, the α-AlF_3 phase. Chupas et al. have described the structures of the aluminum fluoride allotropic forms by taking into account simple building units $(Al-F-)_n$, where n is the

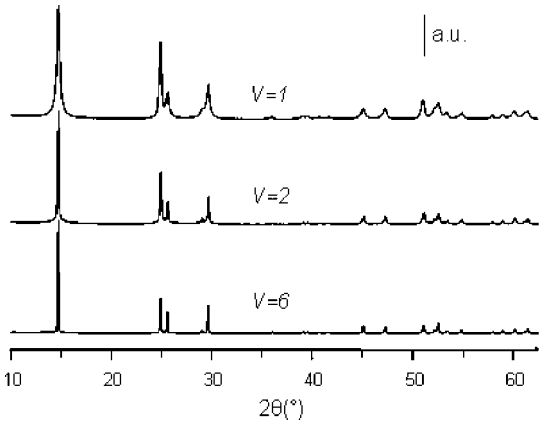

Figure 6. Dependence of the X-ray diffraction powder pattern with the volume ratio of solvents $V = V_{water}/V_{isopropanol}$.

number of units forming the ring.[25] Table 1 summarizes the building units present in the α, β, and pyrochlore phases with the corresponding Al−X−Al angles. β-AlF_3 exhibits three- and six-membered rings in the *a*, *b* plane, as well as four-membered rings in the *b*, *c* plane.The α-AlF_3 phase exhibits four-membered rings, whereas the pyrochlore presents three- and six-membered rings. Thus, hydroxyl groups, because of the presence of hydrogen atoms, favor small Al−X−Al (X = F or OH) angles, as typically found in the three-membered rings. This assumption is consistent with our observation that an increase in the [HF] content leads to the following sequence: pyrochlore → β-$AlF_{3-x}(OH)_x$ → α-AlF_3. Low [HF] contents favor small Al−X−Al angle, as found in the three- and six-membered rings of the pyrochlore phase. When passing from the pyrochlore to the β phase, the number of hydroxyl groups decreases, and conversely, the Al−X−Al angles of the three- and six-membered rings increase. The appearance of four-membered rings in the β phase corresponds to an even higher Al−X−Al angle of 166°. Finally, the α-AlF_3 network shows Al−X−Al angles of only 158°, lower than the four-membered ring angle found in the β form but larger than the three- and six-membered rings, because the framework consists of a denser packed stacking. Therefore, by tuning the [HF]/[Al] precursor molar ratio, a correlation between the types of the building units, the Al−X−Al angle and the OH/F final content can be established.

3.1.3. Influence of the Solvent Ratio: Monitoring the Surface Area by Limiting the Crystallization Kinetics. As shown previously, pure HTB phase can be obtained using nitrate as Al precursor and a [HF]/[Al] precursor molar ratio equal to 3. To get high-surface-area materials, we have tuned the volume ratio of the used solvents $V = V_{water}/V_{isopropanol}$, ranging from $V = 6$ to $V = 1$. The evolution of the powder X-ray diffraction patterns as a function of the volume ratio *V* has been represented in Figure 6. As can be observed, the increase in isopropanol content leads to a broadening of the X-ray diffraction peaks. In a first approximation, this can be ascribed to a decrease in the particle size. This trend was confirmed by measuring the surface area. As revealed by the BET method, the surface area of the materials

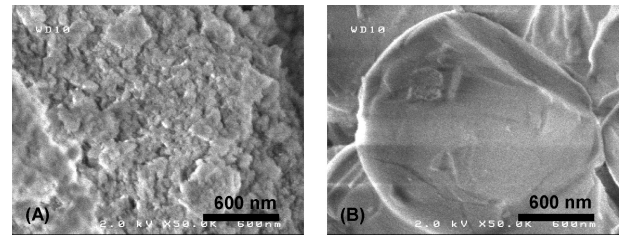

Figure 7. Scanning electron micrographs of (A) high- and (B) low-surface-area β-$AlF_{3-x}(OH)_x$.

Table 2. Surface Areas of β-$AlF_{3-x}(OH)_x$ Materials

sample	water/isopropanol volume ratio	surface area ($m^2\ g^{-1}$)
HSA	1	82
MSA	2	49
LSA	6	3

increases with increasing isopropanol rates and corresponds to 3, 49, and 82 $m^2\ g^{-1}$ for $V = 6$, 2, and 1, respectively. The materials have been named as low (LSA), medium (MSA), and high (HSA) surface area, as reported in Table 2. The effect of the isopropanol on the crystallization growth is clearly highlighted on the scanning electron micrographs represented in Figure 7, illustrating the drastic change in both the particle size and their morphology. Whereas LSA β-$AlF_{3-x}(OH)_x$ exhibits very large particles, HSA β-$AlF_{3-x}(OH)_x$ consists of nanosized particles. Therefore, by varying the solvent medium, we can monitor the surface area, and an aqueous medium favors the crystallization growth, whereas the presence of isopropanol limits its kinetics.

3.2. Structural Investigation of β-$AlF_{3-x}(OH)_x$. *3.2.1. Microstructural Characterization of the High-Surface-Area Material: From Williamson−Hall Approach to Global Profile Refinement.* The microstructural features (coherent domain size and strains) of the samples of the β-$AlF_{3-x}(OH)_x$ series were extracted from the additional broadening of the Bragg peaks with respect to the instrumental one. For our diffractometer, this instrumental contribution to the line broadening was previously established for XRD patterns of standard LaB_6 powder.

Initial profile matching (Le Bail fit) of the diffraction pattern of HSA β-$AlF_{3-x}(OH)_x$ using an isotropic model of the size and strain line broadening did not gave satisfactory results: $cR_p = 12.8\%$, $cR_{wp} = 15.7\%$, $\chi^2 = 3.96\%$. One can see in Figure 8 that the full width at half maximum (fwhm) of some experimental peaks is smaller than the calculated one, (002), whereas for other lines it is larger, (200), (130). This *hkl*-dependent line broadening suggests some anisotropy related to the sample intrinsic microstrains or crystallite shape.

The following parts will be devoted to the analysis of the anisotropic line broadening and microstructural effects in HSA β-$AlF_{3-x}(OH)_x$. Our approach was based on two integral-breadth methods: Williamson−Hall[26] and whole pattern profile matching.

3.2.1.1. Williamson−Hall Approach. The Williamson−Hall method is a good starting point of the microstructural

(25) Chupas, P. J.; Corbin, D. R.; Rao, V. N. M.; Hanson, J. C.; Grey, C. P. *J. Phys. Chem. B* **2003**, *107*, 8327.

(26) Williamson, G. K.; Hall, W. H. *Acta Metall. Sin.* **1953**, *1*, 22.

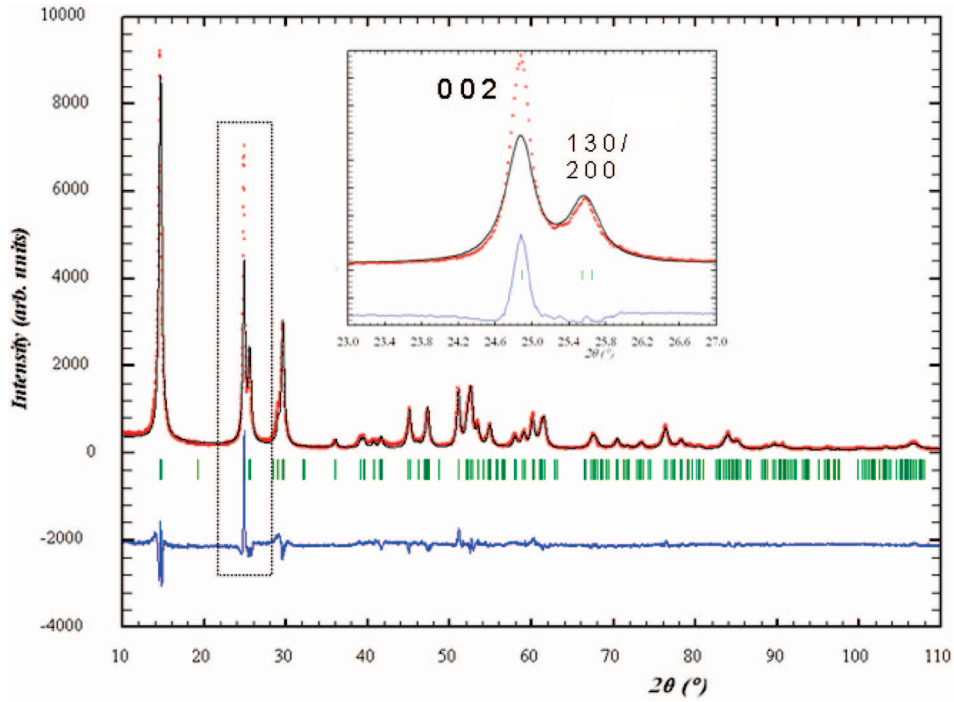

Figure 8. Initial profile matching of the diffraction pattern of HSA β-AlF$_{3-x}$(OH)$_x$ using isotropic model. Experimental X-ray diffraction powder pattern (red curve) compared to the Rietveld-refined profile (black curve) and the difference curve (blue curve). The vertical bars correspond to the positions of the Bragg reflections. Inset: zoom on the (002) reflection line.

characterization because it allows one to identify the relative contribution of each size or strain effects to the broadening of the X-ray diffraction peaks. Here, a simplifying assumption makes all diffraction peaks considered to be Lorentzian. In that case, the observed integral breadth (β_{obs}) can be adjusted for the instrumental broadening contribution (β_{ins}) by a simple substraction of the latter so the sample intrinsic part is obtained: $\beta_{samp} = \beta_{obs} - \beta_{ins}$. Moreover, β_{samp} is the sum of the size and the strain broadening contributions through the following relation: $\beta_{samp} = \lambda/(L \cos \theta) + 4(\tan \theta)\epsilon$ or $\beta_{samp} \cos \theta = A + B \sin \theta$, where $A = \lambda/L$ and $B = 4\epsilon$. So when a diagram $\beta_{samp} \cos \theta = f(\sin \theta)$ is dressed for a number of diffraction peaks, the average crystallite size $\langle L \rangle$ and strains $\langle \epsilon \rangle$ can be easily evaluated from the ordinate at the origin A and the slope B, respectively.

A Williamson−Hall diagram for HSA β-AlF$_{3-x}$(OH)$_x$ was dressed with selected peaks (Figure 9). We focused our attention on the well-resolved lines that could be suitably separated for an individual profile fit. Among them are some of the most badly fitted ones by the isotropic size and strain broadening model (Figure 8). Despite the limited number of data for the Williamson−Hall diagram, two series of points are distinguished, each one being fitted with a linear regression. The first one is related to (00l) line (or at least line l-index high toward h and k), and the second one to the (hk0) lines. The two fits are parallel, so one has to consider the strain-related contribution to the line broadening as being isotropic. On the other hand, the plot gives good evidence for anisotropic size-related broadening of the Bragg peaks. The large peaks overlap in the diffraction pattern makes the (h00) and (0k0) lines absent from our Williamson−Hall diagram. So the determination of the anisotropy direction is rather tricky

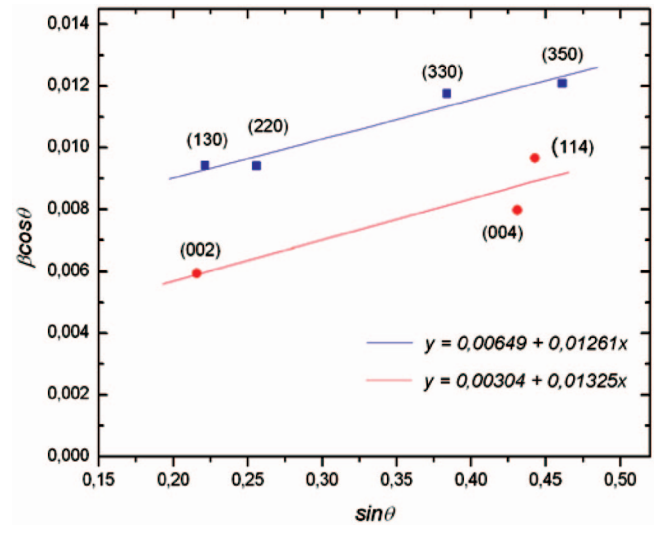

Figure 9. Williamson−Hall plots of HSA β-AlF$_{3-x}$(OH)$_x$.

with regard to the orthorhombic symmetry of the unit cell. However, the (00l) lines being sharper, this is an indication for a large domain size along the [001] direction. The simplest shape model compatible with that observation is a needle along the c axis. The approximate values of the limit dimensions deduced from the Williamson−Hall diagram correspond to a $\langle L00l \rangle / \langle Lhk0 \rangle$ ratio around 2.

3.2.1.2. Global Profile Refinement. This method offers the possibility to get a much more fine analysis of the microstructure and to calculate accurate values for the microstrains and the crystallite size.[27] The peak profiles are fitted using the pseudo-Voigt function of Thompson−Cox−Hastings,[28] which allows refining separately the angular dependence of both Lorentzian (H_L) and Gaussian (H_G) components of fwhm. So, for a given diffractometer with

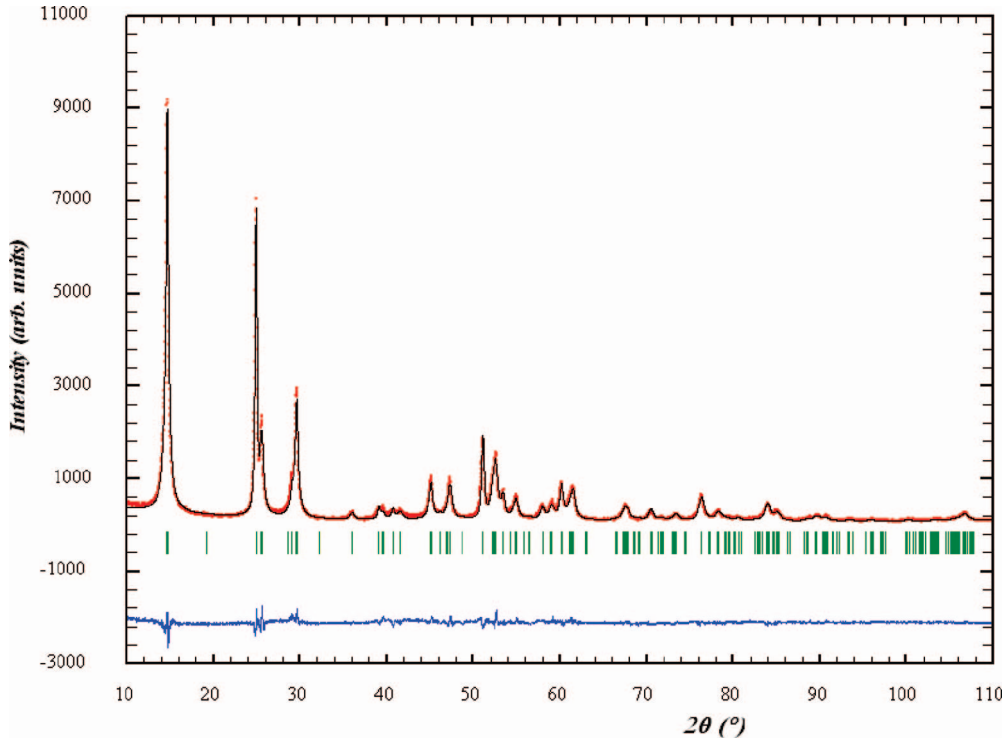

Figure 10. Final profile matching of the diffraction pattern of HSA β-$AlF_{3-x}(OH)_x$ using an anisotropic size model, i.e., platelet running in the *b*, *c* plane. Experimental X-ray diffraction powder pattern (red curve); Rietveld-refined profile (black curve), and difference curve (blue curve). The vertical bars correspond to the positions of the Bragg reflections.

previously defined instrumental resolution function, the sample contributions to the line profile are calculated as follows

$$H_G^2 = (U_{\text{strain\_iso}} + (1-\xi)^2 D^2_{\text{strain\_aniso}}) tg^2\theta + \frac{G_{\text{size\_iso}}}{\cos^2\theta}$$

$$H_L = (X_{\text{strain\_iso}} + \xi D_{\text{strain\_aniso}}) tg\theta + \frac{Y_{\text{size\_iso}} + F_{\text{size\_aniso}}}{\cos\theta}$$

where $U_{\text{strain\_iso}}$, $X_{\text{strain\_iso}}$, $G_{\text{size\_iso}}$, and $Y_{\text{size\_iso}}$ are refinable parameters related to an isotropic strain and size broadening effects, whereas $D_{\text{strain\_aniso}}$ and $F_{\text{size\_anizo}}$ are analytical functions for the *hkl*-dependent model. ζ is a mixing coefficient for the Lorentzian part of strains. The integral method is finally applied to calculate apparent crystallite size and strains in the sample.

The whole profile matching of the diffraction pattern of HSA β-$AlF_{3-x}(OH)_x$ was resumed using different anisotropic size broadening models. The first to be applied was the needlelike model, suggested by the Williamson−Hall analysis, and it was not successful. Satisfactory refinement was reached when using a platelet-shaped model with the short dimension along the *a* axis ($cR_p = 7.8\%$, $cR_{wp} = 9.7\%$, $\chi^2 = 1.5\%$). The final fit is displayed in Figure 10. This result is perfectly compatible with the Williamson−Hall plot because it defines the largest values for the domain size along the [00*l*], [0*k*0], and [0*kl*] directions. The calculated limit dimensions of the platelet crystallites are 8 nm along the *a* axis and 34 nm in the *b*, *c* plane. The average particle size was 15 nm. The microstrains, for their part, were refined within an isotropic model and the calculated average value is $\epsilon = 2.2 \times 10^{-3}$.

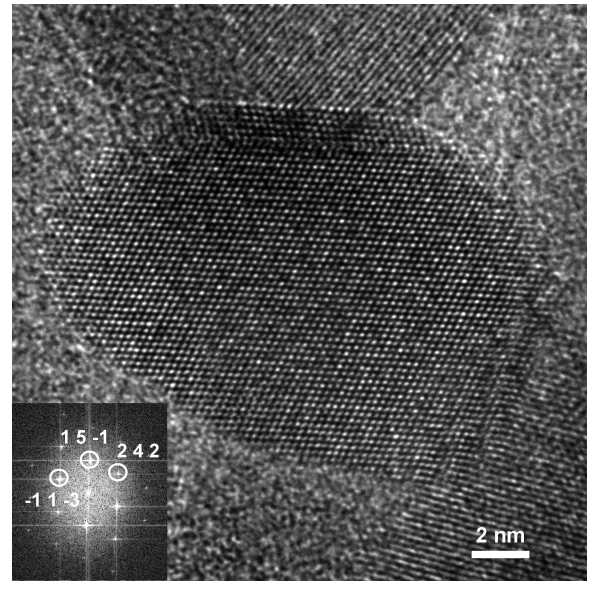

Figure 11. HRTEM image of an HSA β-$AlF_{3-x}(OH)_x$ particle with [−723] zone axis. The corresponding Fourier transform is given in the inset.

3.2.1.3. Transmission Electron Microscopy. High-resolution transmission microscopy experiments were performed on the HSA material, and Figure 11illustrates a HRTEM image of a particle typically observed during HRTEM investigation. The corresponding Fourier transform performed on the particle is shown on the inset of the Figure

(27) Rodriguez-Carvajal, J.; Roisnel, T. Line broadening analysis using Fullprof: determination of microstructural properties. *Proceedings if the 8th European Powder Diffraction Conference*, Uppsala, Sweden, May 23−26, 2002; Trans Tech Publication: Zurich, Switzerland, 2002.
(28) Thompson, P.; Cox, D. E.; Hastings, J. B. *J. Appl. Crystallogr.* **1987**, *20*, 79.

Table 3. Rietveld Refinement Results

sample	cell parameters (Å)	B_{iso} (Å^2)	cR_p (%)	cR_{wp} (%)	R_{Bragg} (%)	χ^2 (%)
HSA	6.9681(2) 12.0360(3) 7.1434(1)	Al^{3+}: 0.79(3); F^-:0.83(3)	11	13.2	4.1	2.96
LSA	6.9494(4) 12.0352(6) 7.1328(8)	Al^{3+}: 0.62(3); F^-:1.25(4)	22.6	24.2	8.8	3.85

Table 4. Comparison of Crystallographic Data of HSA and LSA β-AlF$_{3-x}$(OH)$_x$ with Those of β-AlF$_3$

interatomic distances (Å), bond angles (deg)	HSA-AlF$_{3-x}$(OH)$_x$	LSA-AlF$_{3-x}$(OH)$_x$	β-AlF$_3$
Al2−F1	2 × 1.857(12)	2 × 1.83(3)	2 × 1.800(1)
Al1/Al2−F2	4 × 1.77(3)/2 × 1.82(2)	4 × 1.81(8)/2 × 1.78(9)	4 × 1.801(1)/2 × 1.800(1)
Al1−F3	2 × 1.789(5)	2 × 1.787(6)	2 × 1.796(1)
Al2−F4	2 × 1.804(8)	2 × 1.803(9)	2 × 1.798(1)
Al2−F1−Al2	139.4(5)	143.7(12)	148.7
Al1−F2−Al1	151.9(11)	151.0(4)	148.3
Al1−F3−Al1	173.1(2)	172.3(3)	166.4
Al2−F4−Al2	163.8(4)	162.9(4)	165.5

11, and the zone axis particle has been indexed as [−723]. Because of the high *h* values and low *k* and *l* ones, this zone axis can be assimilated to [*h*00] type. This is consistent with the model used for X-ray diffraction analysis, i.e., a platelet model perpendicular to the a direction. Finally, one should have to point out that the particle size that can be associated to a (0*kl*) plane is in the range of that determined by refinement, i.e., 13–18 nm.

3.2.2. Probing the Anionic Environment by Rietveld Refinement and NMR Spectroscopy: OH/F Ordering. As previously quoted, the β phase adopts the *Cmcm* space group,[3c] in which Al atoms occupy two crystallographic sites Al1 and Al2, in the 4b and 8d Wyckoff positions, respectively. In addition to the different multiplicity, Al1 and Al2 also differ on the type of anionic environment. Al1 is surrounded by four F2 and two F4, whereas Al2 is surrounded by two F3, two F1, and two F2, which link both aluminum atoms. F3 and F4 fluorine atoms form the four-membered rings, which are related to the building unit presents in α-AlF$_3$, whereas F1 and F2 atoms described the six-membered rings.

Crystalline structures of HSA and LSA β-AlF$_{3-x}$(OH)$_x$ were refined by the Rietveld method. Some refinement results are summarized in Table 3.

Interatomic Al−X (X = OH, F) distances found in aluminum fluorides differ from those in hydroxyfluorides phases: 1.797 and 1.842 Å in α-AlF$_3$ and pyrochlore AlF$_{1.5}$(OH)$_{1.5}$ phases, respectively.[3a,3b]

In an attempt to localize the hydroxyl groups inside peculiar crystallographic sites of the HTB framework, some refined interatomic distances and angles of HSA and LSA β-AlF$_{3-x}$(OH)$_x$ are displayed in Table 4 and are compared with those of the free-hydroxyl compound β-AlF$_3$. Atomic positions are available in the Supporting Information. In both samples, the two F3 and F4 anionic crystallographic sites present interatomic distances in the range of those found in β-AlF$_3$. These sites can thus be considered as fully fluorinated. On the contrary, the large estimated standard deviations observed for interatomic distances relative to F1 and F2 sites show that the structures should present a heterogeneity of distances, which depends on the nature of the anion occupying these sites. The long Al−F1 distance found in the case of HSA β-AlF$_{3-x}$(OH)$_x$ should account for the location of OH groups in this site (Table 4). Therefore, in both samples, sites F1 and F2 can thus be considered as partially hydroxylated. As explained previously, the presence of hydroxyl groups tend to favor small Al−X−Al angles. In both HSA and LSA β-AlF$_{3-x}$(OH)$_x$, the Al2−F1−Al2 angle (Table 4) is smaller than those found in hydroxyl-free β-AlF$_3$, confirming the presence of OH groups in this site. On the contrary, the Al1−F2−Al2 angle is larger than that found in β-AlF$_3$. This can be explained considering that the strain induced by the small Al2−F1−Al2 angle should be compensated by the relaxation of the Al1−F2−Al2 angle, because a decrease in both angles should lead to the destabilization of the structure. Nevertheless, the F2 site should probably contain fewer OH species than the F1 one.

To probe the F/OH anionic repartition and the cationic disorder, we have used ^{19}F and ^{27}Al MAS NMR spectroscopies for both LSA and HSA samples.

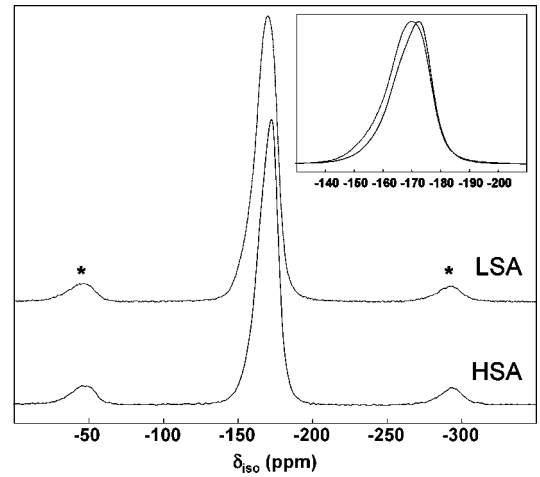

Figure 12. ^{19}F MAS NMR spectra of LSA and HSA at 34 kHz. The star symbols indicate the spinning sidebands.

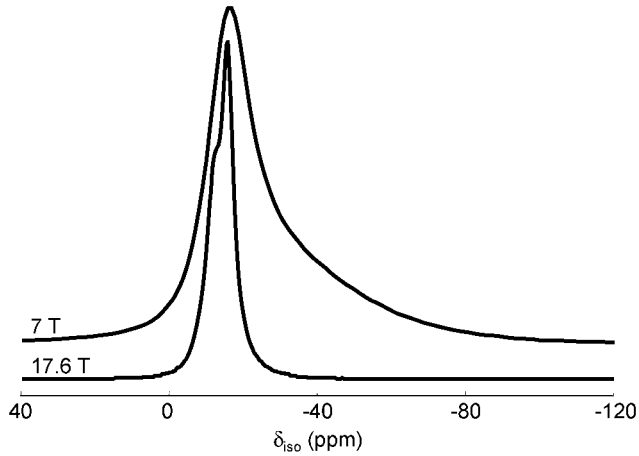

Figure 13. Central transition of the[27] Al NMR spectra of the LSA sample recorded at 7 and 17.6 T.

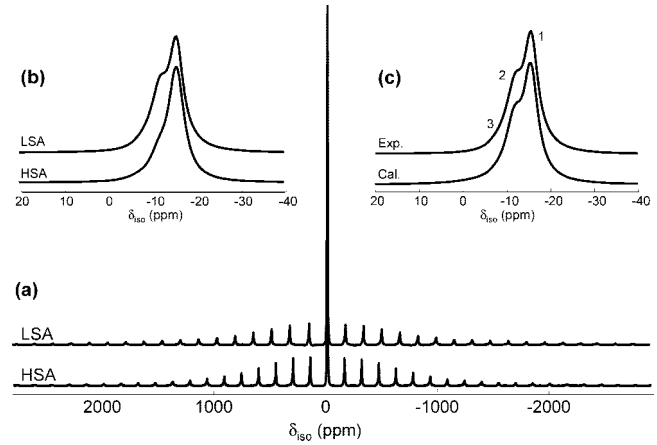

Figure 14. (a) Experimental[27] Al NMR spectra of LSA and HSA, recorded at 17.6 T, at spinning rates of 32 and 30 kHz, respectively. (b) Central transition of both compounds. The reconstruction of the central transition of the LSA sample using three contributions is presented in (c).

^{19}F MAS NMR spectra of LSA and HSA, displayed in Figure 12, show one broad peak. Despite the existence of four different fluorine sites for each sample, the spectra were reconstructed using three contributions whose characteristics are gathered in the Supporting Information. The widths of the resonances (2–6 kHz) mirror the chemical shift distribution related to the disorder around fluorine atoms in these compounds. The lowest δ_{iso} values may be related to fluorine atoms in AlF_6^{3-} octahedra (δ_{iso} (^{19}F in α- and β-AlF_3) = −172[29]). As already observed,[25,29–36] ^{19}F chemical shifts of octahedral aluminum environments with oxygen and fluorine in the first coordination sphere increase with the oxygen content. Despite identical chemical formula for the two compounds, it can be noticed that the δ_{iso} values increase from HSA to LSA sample (Figure 12), which may indicate a more important OH/F ratio in the LSA sample.

^{27}Al MAS NMR spectra of HSA and LSA materials recorded at 7 and 17.6 T are shown in Figure 13. The full spinning sideband manifold is featureless (Figure 14), indicating a distribution of quadrupolar coupling constants (QCCs) supported by the characteristic tail of the central transition of the 7 T spectra (Figure 13). The high magnetic field reduces the influence of the quadrupolar interaction contribution to the spectrum, allowing resolution of ^{27}Al resonances with close δ_{iso} values. Deconvolution of both spectra shown in Figure 14c for the LSA sample and in the Supporting Information for the HSA sample is achieved with three Gaussian lines (see Experimental Section) whose features are gathered in Table 5. The chemical shifts range from −15.5 to −7.7 ppm, characteristic of a 6-fold coordinated aluminum ion. It can be reminded that pure aluminum fluorides, α- and β-AlF_3, exhibit resonances at −16 and −15 ppm, respectively.[29,37] The appearance of peaks at higher chemical shifts is assigned to the occurrence of oxygen in the vicinity of Al^{3+} ions.[25,29,30,32–36] For LSA and HSA β-$AlF_{3-x}(OH)_x$, the $\nu_{Q\eta}$ values are higher than that of β-AlF_3 (132 kHz).[29] Moreover, the $\nu_{Q\eta}$ values increase with the number of OH groups in the vicinity of Al^{3+} ions (Table 5), in agreement with a more disordered environment. One can notice larger $\nu_{Q\eta}$ values for HSA. The higher surface area may give rise to more distorted $AlF_{6-x}(OH)_x$ octahedra.

As shown in Figure 14 and Table 5, the peaks at higher chemical shifts have a higher relative intensity in the LSA sample than in the HSA sample, in contradiction with the proposed identical chemical formula. This discrepancy is ascribed to the difficulty to accurately determine the OH/F ratio in those compounds. To quantify the various possible $AlF_{6-x}(OH)_x$ environments, we considered three compositions that remain within the uncertainty on compositions given by chemical analyses: $AlF_{2.6}(OH)_{0.4}$, $AlF_{2.5}(OH)_{0.5}$, and $AlF_{2.4}(OH)_{0.6}$. On the basis of a random F/OH distribution occurring on F1 and F2 sites, the various possible environments are $AlF_2F'_{4-x}(OH)_x$ with F = F3 or F4 and F′ = F1 and/or F2 (Figure 1) whose probabilities of occurrence are given for the three compositions in Table 6 taking into account a binomial law. If we assume that AlF_6 and $AlF_5(OH)$ species give rise to the main peak observed at −15.5 ppm, the chemical composition of the HSA material would be $AlF_{2.6}(OH)_{0.4}$. This sample contains 82% AlF_6 and $AlF_5(OH)$, 16% $AlF_4(OH)_2$, and 2% $AlF_3(OH)_3$ species. On the other hand, for LSA compound, the chemical composition $AlF_{2.4}(OH)_{0.6}$ gives the best agreement with the ^{27}Al NMR line intensities (Table 5).

(29) Chupas, P. J.; Ciraolo, M. F.; Hanson, J. C.; Grey, C. P. *J. Am. Chem. Soc.* **2001**, *123*, 1694.
(31) Simon, N.; Guillou, N.; Loiseau, T.; Taulelle, F.; Férey, G. *J. Solid State Chem.* **1999**, *147*, 92.
(32) Fischer, L.; Harlé, V.; Kasztelan, S.; d'Espinose de la Caillerie, J.-B. *Solid State Nucl. Magn. Reson.* **2000**, *16*, 85.
(33) Dumas, E.; Taulelle, F.; Férey, G. *Solid State Sci.* **2001**, *3*, 613.
(34) Zhou, B.; Sherriff, B. L.; Taulelle, F.; Wu, G. *Can. Mineral.* **2003**, *1*, 891.
(35) Chupas, P. J.; Grey, C. P. *J. Catal.* **2004**, *224*, 69.
(36) Kemnitz, E.; Groβ, U.; Rüdiger, St.; Scholz, G.; Heidemann, D.; Troyanov, S. I.; Morosov, I. V.; Lemée-Cailleau, M.-H. *Solid State Sci.* **2006**, *8*, 1443.
(37) Silly, G.; Legein, C. Buzaré, J.-Y.; Calvayrac, F. *Solid State Nucl. Magn. Reson.* **2004**, *25*, 241.
(30) Taulelle, F.; Pruski, M.; Amoureux, J. P.; Lang, D.; Bailly, A.; Huguenard, C.; Haouas, M.; Gérardin, C.; Loiseau, T.; Férey, G. *J. Am. Chem. Soc.* **1999**, *121*, 12148.
(38) Zhou, B.; Sherriff, B. L.; Hartman, J. S.; Wu, G. *Am. Mineral.* **2007**, *92*, 34.
(39) Scheurell, K.; Scholz, G.; Kemnitz, E. *J. Solid. State Chem.* **2007**, *180*, 749.

Table 5. Line Label, Isotropic Chemical Shift δ_{iso}, Quadrupolar Product $\nu_{Q\eta}$ (kHz), and Relative Line Intensity (%) Deduced from the Reconstruction of the^{27} Al MAS NMR Spectra (see Experimental Section) of the LSA and HSA Samples, and Assignment of the^{27} Al NMR Lines

	LSA			HSA		
line	1	2	3	1	2	3
δ_{iso} (ppm)	−15.5	−11.7	−7.7	−15.5	−11.7	−9.5
$\nu_{Q\eta}$	250	530	840	280	610	990
relative intensity	64	33	3	82	16	2
assignment	AlF_6 and $AlF_5(OH)$	$AlF_4(OH)_2$	$AlF_3(OH)_3$	AlF_6 and $AlF_5(OH)$	$AlF_4(OH)_2$	$AlF_3(OH)_3$

Table 6. Probability of Occurrence of the $AlF_{6-x}(OH)_x$ species, Based on a OH/F Distribution on F1 and F2 sites, OH Content Being Equal in Both Al1 and Al2 sites

chemical composition	P_F[a]	AlF_6 (%)	$AlF_5(OH)$ (%)	$AlF_4(OH)_2$ (%)	$AlF_3(OH)_3$ (%)	$AlF_2(OH)_4$ (%)[b]
$AlF_{2.6}(OH)_{0.4}$	0.8	41	41	15	3	N
$AlF_{2.5}(OH)_{0.5}$	0.75	32	42	21	5	N
$AlF_{2.4}(OH)_{0.6}$	0.7	24	41	26	8	1

[a] P_F, probability of having a fluorine atom on F1/F2 sites. [b] N, negligible.

This result supports the assumption deduced from the ^{19}F spectra for a higher OH/F ratio in the LSA sample. The higher number of OH groups in LSA β-$AlF_{3-x}(OH)_x$ may explain the poor agreement factor ($R_{Bragg} = 8.8\%$), the large estimated standard deviations observed for Al−F1/F2 distances as well as the high thermal parameter (B_{iso}, Table 3) found for the anionic sites. The ^{27}Al NMR study thus confirms the localization and the statistic distribution of the OH groups in F1 and F2 sites.

Conclusion

The synthesis of aluminum hydroxyfluorides derived from β-AlF_3 has been achieved using microwave-assisted synthesis. The choice of the aluminum precursor, the solvents, and the HF/Al molar ratio are essential in order to get nanosized β-$AlF_{3-x}(OH)_x$. As far as the aluminum precursor is concerned, a secondary reaction occurring during the microwave-assisted synthesis has been identified and involves the reduction of nitrate into ammonium groups coupled with the oxidation of isopropanol. The HF content has been proved to be decisive on the nature of the final allotropic forms. Three various structures can be stabilized corresponding to pyrochlore, HTB, and α-ReO_3 networks, which will be detailed in forthcoming papers. This opens a new pathway for the preparation of aluminum-based fluorides exhibiting high surface area, which in the case of the HTB phase has been monitored as a function of the water/isopropanol volume ratio. X-ray diffraction analysis using the Rietveld method has revealed a platelet shape for the prepared crystallites. NMR spectroscopy has proved to be a powerful tool to probe and quantify the various $AlF_{6-x}(OH)_x$ environments. Furthermore, this technique supports the localization and the statistic distribution of the OH groups in F1 and F2 sites and allows stating more precisely the chemical compositions. The presence of OH groups inside the HTB network seems to strongly perturb the framework as revealed by the difficulty to get accurate Al−X distances. Finally, FTIR spectroscopy has shown the presence of strong Lewis acid sites by NH_3 adsorption. The acidic properties of the nanosized β-$AlF_{3-x}(OH)_x$ are currently studied by adsorption of probe molecules (pyridine, CO, ^{36}Cl radiotracers) and will be discussed in a forthcoming paper.[40]

Acknowledgment. We thank the EU for financial support through the 6th Framework Programme (FUNFLUOS, Contract NMP3-CT-2004-5005575). Lydia Raison is gratefully acknowledged for performing EMPA analysis.

Supporting Information Available: Atomic positions of LSA and HSA; ^{19}F MAS NMR experimental and calculated spectra of LSA and HSA; ^{19}F NMR spectrum reconstruction parameters; and experimental and calculated central line of the ^{27}Al MAS NMR spectra of LSA and HSA (PDF). This material is available free of charge via the Internet at http://pubs.acs.org.

CM702603B

(40) Dambournet, D.; Vimont, A.; Leclerc, H.; Lavalley, J. C.; Daturi, M.; Durand, E.; Winfield, J. M.; Tressaud, A.; Demourgues, A. Submitted.